Evaluation of methods using topology and integral geometry to assess wettability

Martin J. Blunt *, Takashi Akai, Branko Bijeljic
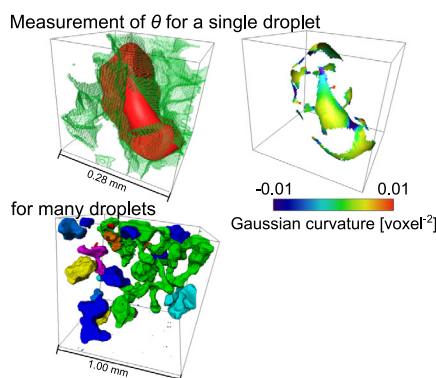
Department of Earth Science and Engineering, Imperial College London, London SW7 2BP, UK

GRAPHICAL ABSTRACT

We relate the integral of Gaussian curvature over a fluid meniscus to contact angle using concepts in integral geometry.

$$2\pi n(1 - \cos\theta) = 4\pi - \int \kappa_{G12} dS_{12},$$

where n is the number of contact loops, θ is the contact angle, and κ_{G12} is the Gaussian curvature of the fluid meniscus which is integrated over its surface, S_{12}.

Measurement of θ for a single droplet

for many droplets

Gaussian curvature [voxel^{-2}]

-0.01   0.01

0.28 mm

1.00 mm

ARTICLE INFO

ABSTRACT

Hypothesis: The development of high-resolution *in situ* imaging has allowed contact angles to be measured directly inside porous materials. We evaluate the use of concepts in integral geometry to determine contact angle. Specifically, we test the hypothesis that it is possible to determine an average contact angle from measurements of the Gaussian curvature of the fluid/fluid meniscus using the Gauss-Bonnet theorem.

Theory and simulation: We show that it is not possible to unambiguously determine an average contact angle from the Gauss-Bonnet theorem. We instead present an approximate relationship: $2\pi n(1 - \cos\theta) = 4\pi - \int \kappa_{G12} \, dS_{12}$, where n is the number of closed loops of the three-phase contact line where phases 1 and 2 contact the surface, θ is the average contact angle, while κ_{G12} is the Gaussian curvature of the fluid meniscus which is integrated over its surface S_{12}. We then use the results of pore-scale lattice Boltzmann simulations to assess the accuracy of this approach to determine a representative contact angle for two-phase flow in porous media.

Findings: We show that in simple cases with a flat solid surface, the approximate expression works well. When applied to simulations on pore space images, the equation provides a robust estimate of contact angle, accurate to within 3°, when averaged over many fluid clusters, although individual values can have significant errors because of the approximations used in the calculation.

1. Introduction

The recent development of advanced imaging and analysis tools has enabled the sophisticated description of flow in porous

* Corresponding author.
E-mail address: m.blunt@imperial.ac.uk (M.J. Blunt).

materials at the pore, or micron, scale [1,2]. One topic of active interest is the assessment of wettability, contact angle, within the pore space [3], often associated with estimates of interfacial curvature [4]. Recent work has developed a suite of analysis techniques to measure contact angle automatically [5–10] and, combined with the determination of curvature, has been used to quantify wettability and capillary pressure [4,11–13].

Two approaches can be used to determine contact angle. The first is geometric, in that the angle that the fluid/fluid meniscus makes with the solid is determined directly from the image [3]. This method has the advantage of being straightforward whilst automatic methods can generate millions of point values from billion-voxel images [14]. There are two limitations, however. The first is that at the three-phase contact line, the identification and segmentation of the three phases (two fluids and the solid) is uncertain, which can lead to errors in the estimates, depending on image resolution, with a tendency for the values to approach 90° (see, for instance [15–18]). The second concern is that, even if accurately determined, these angles may represent hinging values on a rough or altered-wettability surface so are not necessarily the correct angles to use to characterize displacement or as input into pore-scale models [15].

The other approach is to use an energy balance [15,19]. This has the advantage of finding the contact angle associated with displacement, but also suffers from two possible drawbacks. Firstly, it is based on quantifying differences in fluid configurations to find an average value, rather than finding local variations in wettability. However, simulation studies have shown that it is possible to find the contact angle on a pore-by-pore basis when individual displacement events are confined to a single pore region [20]. Secondly, the energy balance does not consider viscous dissipation and is therefore inaccurate for drainage processes with Haines jumps [21], although this effect can be included in the analysis [20].

Recently, concepts in topology and integral geometry have suggested a powerful approach to the analysis of multiphase flow in porous media [22,23]. Sun et al. [17,24] have used the Gauss-Bonnet theorem to derive an effective macroscopic contact angle θ^{macro} to study the relationship between intrinsic, advancing and receding angles on rough surfaces. Sun et al. [17] showed that θ^{macro} was close to the average contact angle measured automatically [5] within a water-wet sandstone. This approach is, potentially, a major advance, allowing an accurate estimation of contact angle inside porous materials, grounded on fundamental topological principles.

In this paper we first explore the use of the Gauss-Bonnet theorem to determine contact angle, inspired by the work of Sun et al. [17,24]. It is not possible to uniquely associate an average angle with surface integrals of Gaussian curvature of fluid interfaces and the Euler characteristic of fluid clusters. This is because the orientation of the three-phase contact line relative to the fluid/fluid and fluid/-solid interfaces is, in general, not uniform along the three-phase contact line. However, we do suggest an approximate relation, consistent with the work of Sun et al. [17], under certain assumptions. We then explore the use of this relationship using simulated distributions of fluids in the pore space, for which the configurations can be determined accurately and where the wettability is known.

2. The Gauss-Bonnet theorem and contact angle

2.1. External angles of a polygon and curvature

We will start with a pedagogic presentation of topology relevant to flow in porous media for readers who are unfamiliar with the subject (see, for instance, [25] for further reading). Fig. 1 shows a polygon: the sum of the external angles is $2\pi : \sum_{i=1}^{n} \alpha_i = 2\pi$

where we have n external angles α_i. Note that this relationship holds even for a concave polygon, where the angles in the concavity are negative (for example α_4 in Fig. 1). If we have a smooth shape, without corners, there is a similar relationship, if we introduce the concept of curvature, κ. At any point L on a smooth curve, l, a circle can be fitted: the curvature is the inverse of its radius $R, \kappa = 1/R$. Then $\int \kappa \, dl = \int R/R \, du = \int du = 2\pi$ where u is an angular coordinate along l: this will decrease along l in concave regions where the curvature is negative. The final case is a shape which is a combination of smooth and angular regions. The general formula is

$$\int \kappa \, dl + \sum_{i}^{n} \alpha_i \equiv \int du + \sum_{i}^{n} \alpha_i = 2\pi. \tag{1}$$

2.2. The Gauss-Bonnet equation in three dimensions

We now consider the extension of Eq. (1) to three dimensions. Here, we start with a smooth surface bounding a three-dimensional object. The Gauss-Bonnet theorem states [26]
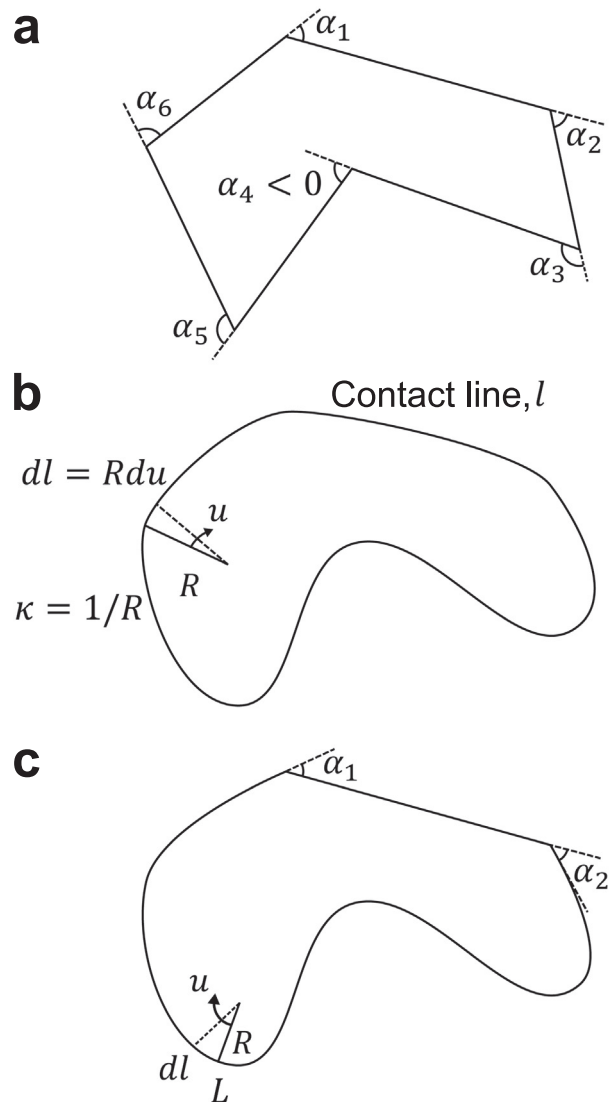

Fig. 1. An illustration of angles and curvatures in two dimensions. (a) For a polygon: $\sum_{i=1}^{n} \alpha_i = 2\pi$. Note that α_4 in a concavity is negative. (b) For a smooth closed loop the equivalent relationship is $\int \kappa \, dl = \int du = 2\pi$. (c) For a two-dimensional shape bounded by straight sides, sharp angles and smooth lines, the generalization of the relationship between curvature and angles is given by Eq. (1).

$$\int \kappa_G \, dS = 4\pi\chi, \tag{2}$$

which provides a relationship between the topology of an object and the integral of the Gaussian curvature across the bounding surface. At any point on a surface we can define two principal curvatures in orthogonal directions, κ_a and κ_b with corresponding radii R_a and R_b respectively. If we consider a sphere of radius R, these two radii are equal: $R_a = R_b = R$; for a cylinder of radius $R, R_a = R$ while $R_b = \infty$. If the surface is saddle-shaped one of the radii of curvature is negative. The Gaussian curvature, $\kappa_G = \kappa_a\kappa_b$, which appears in Eq. (2), is the product of the two principal curvatures: $\kappa_G = 1/R^2$ for a sphere, $\kappa_G = 0$ for a cylinder, while $\kappa_G < 0$ for a saddle. The other term in Eq. (2) is χ, the Euler characteristic which is a measure of the topology of an object: 1 plus the number of holes in the structure minus the number of loops. Thus Eq. (2) relates the integral of the Gaussian curvature of an object to its topology.

Let's take a simple example. A solid sphere has an Euler characteristic of 1 (it has no holes or loops). The surface area of a sphere of radius R is $4\pi R^2$, so the integral of the Gaussian curvatue (which is constant) over this surface is 4π in agreement with Eq. (2). In general though, Eq. (2) is a remarkable result, as it states that however much we distort a sphere (or indeed any object), as long as we do not create holes or loops, the integral of the Gaussian curvature over the surface remains constant.

We will now apply the Gauss-Bonnet theorem to study fluids in a porous medium. First, we will describe the fluid arrangement that we will consider, illustrated in Fig. 2. We have two fluid phases, 1 and 2, separated by a meniscus, described by the surface (or interface) S_{12}. The phases also contact the solid: the three-phase contact line, l, between phases 1, 2 and the solid forms a closed

loop, and we define a contact angle θ measured through phase 1. The solid surface in contact with phase 2 is S_{2s}. The object we will consider is a blob, cluster or ganglion of phase 2: there is a smooth surface between the two fluid phases, another surface between phase 2 and the solid, and a discontinuity in orientation of the surface at the three-phase contact line – this is encapsulated by the contact angle. We can consider applying Eq. (2) to the cluster of phase 2, where there is an additional contribution to the curvature from the contact line.

Sun et al. [17] derived a version of the Gauss-Bonnet theorem, Eq. (2), as follows:

$$\int \kappa_{G12} \, dS_{12} + \int \kappa_{G2s} \, dS_{2s} + k_d = 4\pi\chi. \tag{3}$$

Here we integrate over both the fluid/fluid meniscus, S_{12}, and the contact of phase 2 with the solid, S_{2s}. There is a final term, k_d, called the deficit curvature which quantifies the additional contribution from the contact line.

Before continuing, we will explain the purpose of this analysis. The direct evaluation of k_d involves an integral along the contact line that – as we show later – requires an estimation of the orientation of this line relative to the fluid/fluid and fluid/solid interfaces, which is similar to what is done to find contact angle directly [5], although even more involved. Hence, it suffers from the same uncertainties and errors in segmentation. What we will look for, as in [17], and discussed in detail later, is a general analytical relationship between k_d and contact angle (or an average value), and then use Eq. (3) to estimate this contact angle from integral of Gaussian curvature over the fluid/fluid meniscus, which
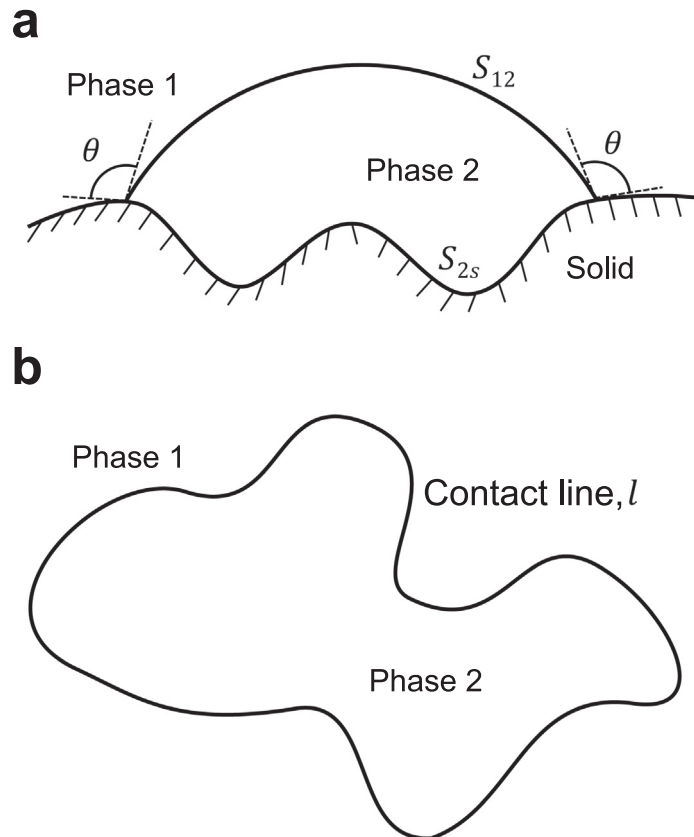

Fig. 2. An illustration of fluid arrangements. We consider two phases, 1 and 2, in contact with a surface. (a) A vertical cross-section showing the surfaces between the two phases S_{12}, and between the solid and phase 2, S_{2s}. The contact angle, which may vary spatially, is θ. (b) A schematic horizontal cross-section with the contact line, l, where the two fluid phases meet the solid.

can be determined with reasonable accuracy from pore-space images [27,18].

2.3. Evaluation of the deficit curvature

Physically the deficit curvature k_d in Eq. (3) accounts for the fact that there is a kink in the surface of the cluster of phase 2 at the three-phase contact line, or a discontinuity in the orientation of a tangent plane to the surface. This is represented geometrically by the contact angle. If the contact angle is 0 (complete wetting) the entire surface (the union of S_{12} and S_{2s}) remains smooth, $k_d = 0$ and Eq. (3) reduces to relating the surface integral of the Gaussian curvature of an unbounded shape to its Euler characteristic, Eq. (2). If the contact angle is not 0, there is a sharp change in orientation of the surface of phase 2 at the contact line, as it passes from contact with phase 1 to the solid.

To evaluate k_d, which from Eq. (2) represents the integral of the Gaussian curvature in the neighbourhood of the contact line, we mathematically smooth the surface in an infinitesimal region as shown in Fig. 3. Locally the surface near the contact line is a patch of a torus: we call this surface S_l. The radius of curvature of the contact line is R at point L, while r is the radius of curvature in the plane perpendicular to the contact line: $R \gg r$ and we can take the limit that $r \to 0$.
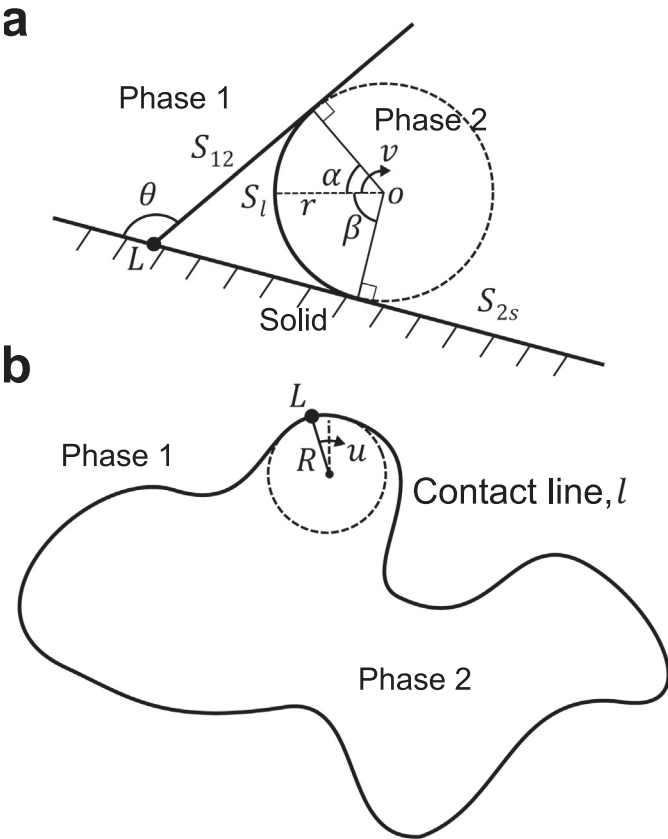

Fig. 3. An illustration of how we compute the curvature associated with the three-phase contact. (a) An enlargement of an arbitrary region close to the contact line at a point L in vertical cross-section. The contact angle θ is indicated. We replace the sharp boundary between S_{12} and S_{2s} at this point with a curved surface of infinitesimal radius of curvature r, S_l, as shown. The horizontal axis lies in the plane of the contact line at L. The angles α and β indicate the orientation of S_{12} and S_{2s} respectively at the three-phase contact. $\theta = \alpha + \beta$. v is the local angular coordinate of the curved interface S_l. (b) A schematic horizontal cross-section of the contact line, l. At point L the radius of curvature in the plane in the neighbourhood of L is R. u is the local angular coordinate.

We first define the geometry local to a point on the three-phase contact line. For convenience we define the plane coincident with the contact line l as horizontal. The contact angle is θ. A line in the vertical plane perpendicular to the meniscus, the surface S_{12}, makes an angle α to the horizontal, while the perpendicular to the solid S_{2s} makes an angle $-\beta$ (as drawn in Fig. 3 it is oriented below the horizontal). Then $\theta = \alpha + \beta$.

On the local torus we define a coordinate system u and v such that a distance increment around the torus in a plane perpendicular to the contact line is $r\,dv$, while it is $R\,du$ parallel to the contact line. A surface element $dS_l = rR\,du\,dv$. Then the deficit curvature k_d, which obeys Eq. (3), can be written as a surface integral of the Gaussian curvature:

$$k_d = \int_0^{2\pi} \int_{-\beta}^{\alpha} \kappa_{Gt} rR \, dv du, \tag{4}$$

where κ_{Gt} is the Gaussian curvature of a torus. This will not be derived here, but it can be shown that [28]:

$$\kappa_{Gt} = \frac{\cos v}{r(R + r\cos v)}. \tag{5}$$

We consider the limit $r \ll R$ such that $\kappa_{Gt} = \cos v / Rr$ and hence Eq. (4) becomes:

$$k_d = \int_0^{2\pi} \int_{-\beta}^{\alpha} \cos v \, dv du = \int_0^{2\pi} \sin \alpha + \sin \beta \, du. \tag{6}$$

We cannot trivially perform the integral over u since α and β may be functions of u in general – the meniscus and solid do not necessarily maintain a constant orientation at the contact line.

Then, recalling that $\theta = \alpha + \beta$, we eliminate α in Eq. (6) using $\sin \alpha = \sin(\theta - \beta) = \sin\theta\cos\beta - \cos\theta\sin\beta$ to obtain:

$$k_d = \int_0^{2\pi} \sin\theta\cos\beta + (1 - \cos\theta)\sin\beta \, du. \tag{7}$$

Eq. (7) shows that there is no unique relationship between the deficit curvature and the contact angle; it also depends on β, the orientation of the contact line and the solid surface. This equation is similar to the expression in [17] (see their Eq. (S9) in the Supplementary Material).

2.4. Testing the Gauss-Bonnet equation on simple examples

To demonstrate the analysis, we will consider three examples illustrated in Fig. 4; in each one the contact angle and orientation β will be constant around the contact line. In this case, from Eqs. (6) and (7), we have:

$$k_d = 2\pi(\sin\alpha + \sin\beta) = 2\pi[\sin\theta\cos\beta + (1 - \cos\theta)\sin\beta]. \tag{8}$$

We have labelled the cases in Fig. 4 such that the angles α and β correspond to the same angles shown in Fig. 3.

The first, easiest, example 1 is a droplet on a flat surface: $\chi = 1$. Here $\beta = \pi/2$ and the Gaussian curvature of S_{2s} is zero. Hence we only consider S_{12} in Eq. (3) to find:

$$k_d = 4\pi - 2\pi(1 - \sin\alpha) = 2\pi(1 + \sin\alpha) = 2\pi(1 - \cos\theta), \tag{9}$$

using $\alpha = \theta - \pi/2$ in this case, which corresponds to Eq. (8).

The second example is when both the meniscus and the solid form parts of spheres. Using simple geometry, the surface area of a sphere of radius r_a to an angle $\pi/2 - \alpha$ to the horizontal, as shown in Fig. 4, is $2\pi r_a^2(1 - \sin\alpha)$. Similarly the area of the portion of the sphere representing the solid is $2\pi r_b^2(1 - \sin\beta)$, where r_b is the radius of the sphere. The Gaussian curvature of the surface, S_{12}, is $1/r_a^2$ and the surface S_{2s} is $1/r_b^2$. Hence we can write Eq. (3) as:
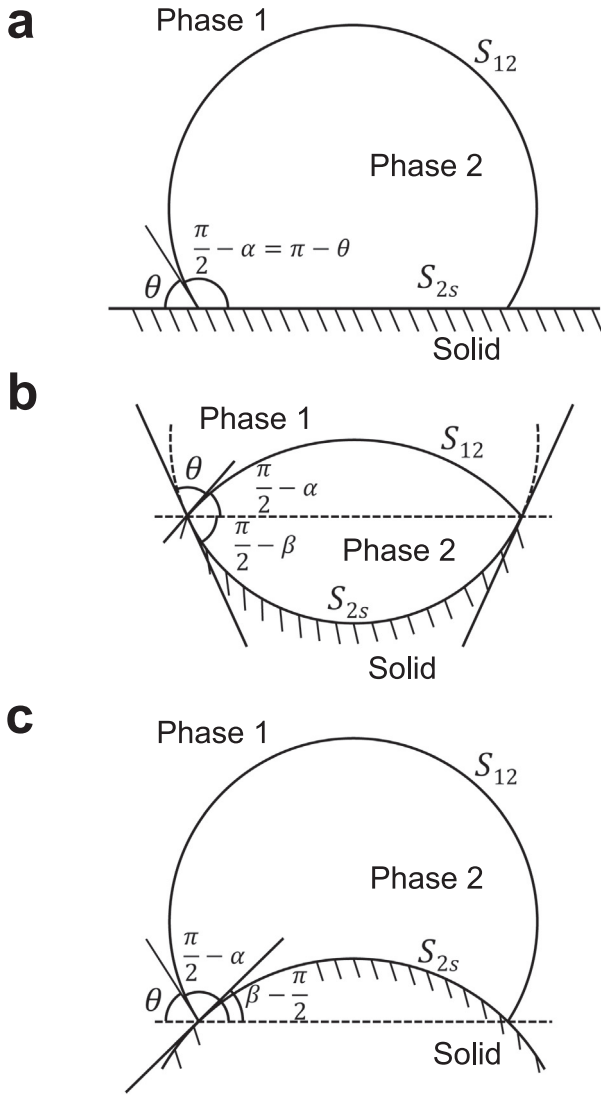
a

b

c

Fig. 4. Three simple examples that we use to determine contact angle from the Gauss-Bonnet theorem. The angles α and β correspond to those shown in Fig. 3. (a) Phase 2 resting on a flat surface. (b) Phase 2 resting on a concave surface. (c) Phase 2 resting on a convex surface, such as the surface of a bead or .spherical grain.

$$\int \kappa_{G12}\ dS_{12} + \int \kappa_{G2s}\ dS_{2s} = 2\pi(2 - \sin\alpha - \sin\beta). \tag{10}$$

The Euler characteristic of the cluster of phase 2 is 1 (the same as a sphere). Hence to agree with Eq. (3):

$$k_d = 4\pi - 2\pi(2 - \sin\alpha - \sin\beta) = 2\pi(\sin\alpha + \sin\beta), \tag{11}$$

which is correct – that is, consistent with Eq. (8) for constant α and β.

In the third example the solid bulges into phase 2: $\alpha < 0$ and $\beta > \pi/2$. We can define $\alpha' = -\alpha$ and $\beta' = \pi - \beta$. Then the areas of S_{12} and S_{2s} are $2\pi r_a^2(1 + \sin\alpha')$ and $2\pi r_b^2(1 - \sin\beta')$ respectively. As before we obtain from Eq. (3):

$$k_d = 4\pi - 2\pi(2 + \sin\alpha' - \sin\beta') = 2\pi(-\sin\alpha' + \sin\beta')$$
$$= 2\pi(\sin\alpha + \sin\beta), \tag{12}$$

which again is consistent with Eq. (8).

2.5. A simple relationship between Gaussian curvature and contact angle

These examples suggest an approximate yet general relationship between Gaussian curvature and contact angle through making three assumptions. (i) We assume that an arbitrary rough surface has, on average, a zero Gaussian curvature, which means that the integral over S_{2s} in Eq. (3) vanishes. (ii) Furthermore, we consider that, on average, the orientation of the contact line is such that β has a mean value of around $\pi/2$. Under these circumstances we have a situation which is a simple generalization of a drop on a flat surface, example 1, with k_d given by Eq. (9). We may have more than one contact line loop, and each one will add to the deficit curvature [17]. This leads to the equation, combining Eq. (9) with Eq. (3):

$$2\pi n(1 - \cos\theta) = 4\pi\chi - \int \kappa_{G12}\ dS_{12}, \tag{13}$$

where n is the number of contact line loops where the single cluster of phase 2 touches the solid. However, as we show later, this does not lead to accurate results. We make one final assumption: (iii) we treat each cluster of phase 2 to be topologically equivalent to a sphere and so $\chi = 1$. This appears to be a strong assertion for complex clusters with holes and loops. We will, in the next section, test these approximations and discuss their implications. If we make these three simplifications, we further simplify Eq. (13) to:

$$2\pi n(1 - \cos\theta) = 4\pi - \int \kappa_{G12}\ dS_{12}. \tag{14}$$

We can use Eq. (14) to estimate an average contact angle for every discrete cluster of phase 2 in a pore-scale image. Since the orientation of the surface is not always flat, the right-hand side of Eq. (14) will tend to be lower than if a flat surface were present: this means that the estimated value of $1 - \cos\theta$ may be smaller than its real value, yielding estimates of θ erroneously close to $\pi/2$ (90°), as encountered when the geometric contact angle is measured [18,14]; on the other hand, consideration of small loops on the surface may tend to underestimate the contact angle. Sun et al. [17], using a sphere on a flat surface (our example 1), identified a macroscopic contact angle θ^{macro} with $\pi(1 - \cos\theta)/2$. They found good agreement with the analytical result when a sufficiently refined surface mesh was used.

3. Assessment and validation using direct numerical simulation

We will demonstrate the use of Eq. (3) and test the accuracy of Eq. (14) using lattice Boltzmann simulations of multiphase flow in porous media. The advantage of using a simulation method is that the results are unaffected by errors or uncertainty in image acquisition and segmentation. We will compute the terms on the right-hand-side of Eq. (14) to estimate the contact angle and compare with the input to the simulations. The lattice Boltzmann method is used with a precise wetting boundary condition to specify local contact angles: details of the approach and validation are presented elsewhere [29,30].

We will consider four cases, Fig. 5:

1. A spherical droplet of phase 2 placed on a flat surface.
2. A spherical droplet of phase 2 placed on a curved solid surface.
3. A ganglion of phase 2 in a triangular capillary.
4. Residual ganglia of phase 2 obtained from simulations of multiphase flow in a beadpack and Bentheimer sandstone.
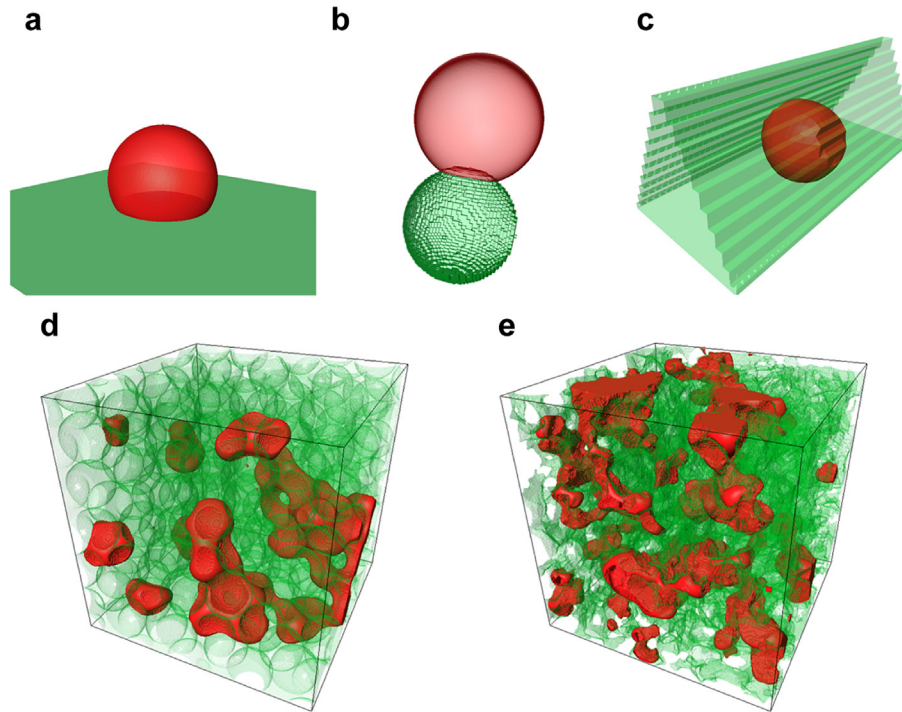
Fig. 5. The four simulation cases used to measure the relationship between contact angle and surface integrals of the Gaussian curvature. (a) Case 1: a spherical droplet placed on a flat surface. (b) Case 2: a spherical droplet placed on a spherical solid grain. (c) Case 3: a droplet in a triangular capillary. (d) Case 4: residual ganglia in pore-space images of a beadpack, and (e) Bentheimer sandstone. Phase 2 and the solid surface are shown in transparent red and green, respectively, while phase 1 is not shown. (For interpretation of the references to colour in this figure legend, the reader is referred to the web version of this article.)

3.1. Simulation conditions

The simulation conditions for the four cases are summarized in Table 1. We used densities and viscosities of $\rho = \rho_1 = \rho_2 = 1000$ kg/m^3 and $\mu = \mu_1 = \mu_2 = 1$ mPa·s respectively, while the interfacial tension between the fluid phases was $\sigma = 25$ mN/m. For the first two cases, we used simple solid geometries where the Gaussian curvature of the interface is analytically determined.

For case 1, in the z-direction, a wall boundary was placed at the top and bottom of the domain, while a periodic boundary condition was applied in the other directions. Initially, a semi-spherical droplet of phase 2 with a radius of 20 lattice nodes was placed at the bottom of the domain, while the rest of the domain was filled with phase 1. For this case we simulated a range of contact angles, similar to the example studied in [30].

For case 2, a spherical solid with a radius of 20 lattice nodes was placed at the lower part of the domain. A periodic boundary condition was applied to the boundaries in all the directions. Initially, a known volume of phase 2 was placed on the spherical solid, while the rest of the domain was filled with phase 1. The simulations were performed until they reached an equilibrium state. For this case we studied contact angles of 60° and 120°, similar to the example studied in [30].

Table 1
Details of the simulation conditions for the four cases studied.

	Ganglion configuration	Voxels	Time steps
Case 1	Flat surface	$101 \times 101 \times 101$	5×10^4
Case 2	Curved surface	$101 \times 101 \times 101$	5×10^4
Case 3	Triangular prism	$49 \times 24 \times 24$	5×10^4
Case 4	Pore-space images	$348 \times 288 \times 288$	$\geqslant 10^6$

For case 3, a cylindrical pore structure with an isosceles triangular cross-section was used of length 175.42 μm (49 lattice nodes), while the triangle side lengths were 71.6 μm, 78.6 μm and 78.6 μm. A periodic boundary condition was applied to the direction perpendicular to the cross-section. Initially, a known volume of phase 2 was placed in the centre of the pore structure, while the rest of the domain was filled with phase 1. The simulations were run until they reached an equilibrium state. For this case we imposed a contact angle of 45°, similar to the example studied in [31].

For case 4, we used two pore structures: a synthetic image of a beadpack and a micro-CT image of a Bentheimer sandstone. The porosity of these structures were 36% for the beadpack, and 21% for Bentheimer sandstone. Porous plates wetting to phases 1 and 2 were placed at $+x$ and $-x$ faces of the porous domain respectively, while the boundaries in the other directions were closed with a solid boundary. We applied a contact angle of 45°. Drainage simulations were performed in the $-x$-direction by gradually increasing the phase 2 pressure through a constant pressure boundary condition at the phase 2-wet porous plate region, while the pressure of phase 1 was maintained constant through a constant pressure boundary condition at the other porous plate. After the simulations reached an irreducible saturation of phase 1, phase 1 was injected in the $+x$ direction by gradually decreasing the pressure of phase 2 while keeping the pressure of phase 1 constant. The simulations were performed until the system reached the residual saturation of phase 2. This simulation condition mimics porous plate capillary pressure measurements in the laboratory. Further details can be found in [20,32].

3.2. Estimation of contact angle

In the simulations, the fluid occupancy in each lattice node was obtained based on a colour function, ρ^N, which takes a value of 1 in

phase 2 and −1 in phase 1, while it takes the value of $−1 < \rho^N < 1$ in the fluid/fluid interface region. Our lattice Boltzmann model is classified as a diffusive interface model which produces a slightly diffusive interface with a thickness of 2 to 3 lattice nodes [20,32]. The exact location of the fluid/fluid interface, S_{12}, is given by a contour surface corresponding to $\rho^N = 0$, which has smoothness below the resolution of the simulation grid.

The solid surface covered with oil was extracted from the simulation results as a triangulated surface. Then we applied 600 iterations of Laplacian smoothing to this surface. This provides sufficient smoothness while maintaining the original shape of a surface [27,31].

The fluid/fluid and fluid/solid interfaces were modelled as triangulated surfaces on which the Gaussian curvature, κ_G, was computed using commercial image analysis software (Avizo). This was performed by fitting a quadratic form to the elemental triangulated surfaces, then the magnitude and direction of the principal curvatures were obtained from the eigenvalues and eigenvectors of the fitted quadratic form [4]. The integral of the Gaussian curvature was obtained by taking an area-weighted summation of κ_G for all the triangulated surface elements.

Table 2 shows a contact angles obtained for cases 1 to 3 where relatively simple geometries were considered. There is good agreement between the input contact angle and the value determined using Eq. (14) when the approximations used in the analysis are valid ($\int \kappa_G dS_{12} = 0$ and $\beta = \pi/2$), namely a flat solid surface oriented in the plane of the contact line, cases 1 and 3. The contact angle can be evaluated within 5°.

For case 2, when we have a curved solid boundary, representing a ganglion on a spherical grain, the use of Eq. (14) does not work, as the assumption of a flat solid surface oriented with the contact line is no longer valid. However, when the full equation is employed, Eq. (3), accounting for the solid curvature, $\int \kappa_G dS_{2s}$, and its orientation, β, with Eq. (8) to find k_d, we can obtain contact angles with similar accuracy to that found for cases 1 and 3.

For case 4, contact angle was determined for residual clusters of phase 2 in the beadpack and Bentheimer sandstone. There were 47 and 78 disconnected ganglia in the beadpack and Bentheimer sandstone, respectively. We chose clusters whose volume was greater than 10^4 voxels for the analysis, resulting in 7 clusters for the beadpack and 17 clusters for Bentheimer sandstone, which accounted for 99% and 97% of the total volume of residual phase 2, respectively. Fig. 6 illustrates the steps taken to perform the analysis for this fourth case, both on a single cluster and for all the clusters in the image. The integral of the Gaussian curvature was calculated on the simulated interface, Fig. 6b and e, while the number of closed contact loops were obtained from the extracted three-phase contact line (boundary voxels of different

phases), Fig. 6c and f. As discussed above we assumed $\chi = 1$ for all the clusters.

Table 3 shows the estimated contact angles for the pore-space images on a cluster-by-cluster basis. It can be seen that for individual ganglia there can be significant errors in the measurement, since the assumptions made in Eq. (14) – a flat surface oriented with the contact line – may not be valid. There is no clear relationship between cluster size and degree of error. However, when averaged over all the ganglia, the contact angle is determined to within 3°, which indicates that this simple approach may indeed provide a valuable average assessment of pore-scale wettability.

3.3. Evaluation of the approximations made

In this section we will critically examine the approximations made in the use of Eq. (14) to estimate contact angle. The first and most obvious assumption is that the Euler characteristic, χ, is 1. As evident from visual inspection of Fig. 6 some ganglia contain loops and hence do not have $\chi = 1$ (the topological equivalent of a solid sphere). We analysed every ganglion and counted the number of loops and holes to calculate χ, which is 1 - the number of loops + the number of holes. We then replaced 4π in Eq. (14) with $4\pi\chi$, Eq. (13): the estimated contact angles are shown in Table 3. What we find is that for all three cases where the Euler characteristic is different from 1, the calculated contact angle is undetermined: this means that $|\cos \theta| > 1$ and so a physical value of θ cannot be found. The reason for this is that we cannot, in these cases, ignore the contribution of the fluid/solid curvature. We can see why this is the case if we consider an example of a cluster containing a hole – a hole that surrounds a solid grain. Then the Euler characteristic is 1 + 1 = 2, adding an additional 4π to the right-hand-side of Eq. (3), which has to be exactly balanced by the integral of the Gaussian curvature around the grain which, from Eq. (2), is 4π. Similarly, for a cluster with a loop, the solid–fluid Gaussian curvature has to provide a negative contribution.

This analysis suggests that we should, instead, consider Eq. (3) in its entirety. This is presented in the final column of Table 3. However, we find that in all but two cases the angle is undetermined; this approach simply does not work on pore-space images. The problem is not the evaluation of the orientation angle β, but the computation of the solid/fluid Gaussian curvature: the undetermined values shown in Table 3 represent cases where regardless of θ and β no physical values can be assigned that enable Eq. (3) to be obeyed.

In our simulations, and indeed from experimental pore-space images, the fluid/fluid interface is, on physical grounds, smooth. Hence it is possible to extract this meniscus and compute its total and Gaussian curvature with reasonable accuracy, as quantified in

Table 2
The results of contact angle obtained for cases 1 to 3. In case 2, the orientation angle of the three phase contact line, β, and the integral of the Gaussian curvature, $\int \kappa_G dS_{2s}$, were analytically obtained based on the input contact angle.

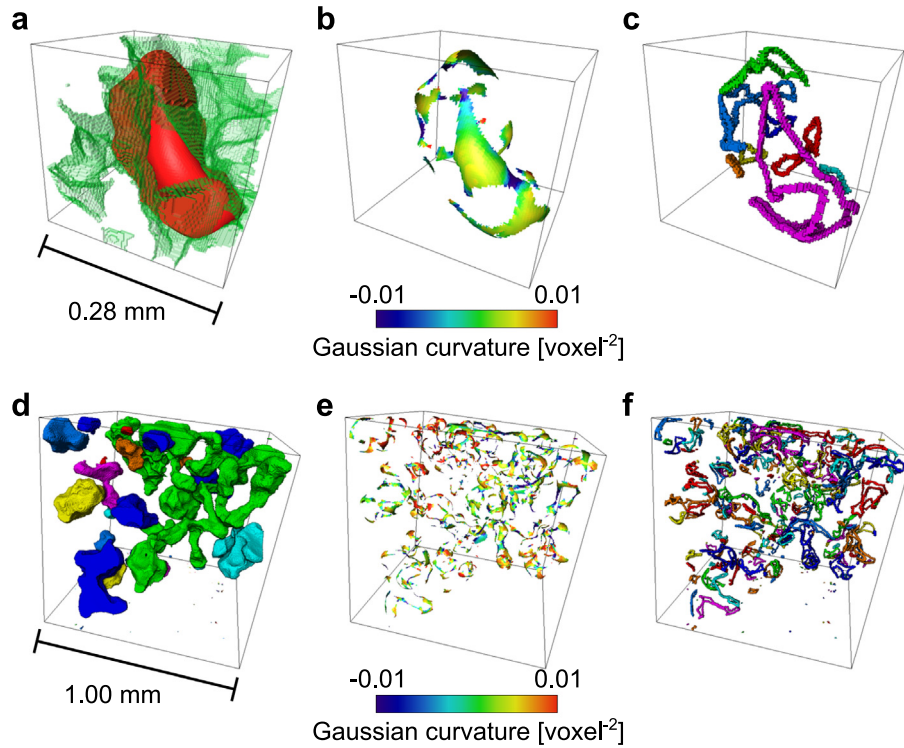| Case	Input θ	β	$\int \kappa_G dS_{2s}$	Estimated θ	
				by Eq. (14)	by Eqs. (3) and (8)
	[degrees]	[degrees]	[−]	[degrees]	[degrees]
Case 1	30.0	90.0	0.0	34.8	34.8
	60.0	90.0	0.0	62.6	62.6
	90.0	90.0	0.0	91.2	91.2
	120.0	90.0	0.0	121.0	121.0
	150.0	90.0	0.0	149.9	149.9
Case 2	60.0	121.5	0.9	32.5	64.0
	120.0	154.6	3.6	57.4	122.1
Case 3	45.0	90.0	0.0	48.0	48.0

Fig. 6. The analysis steps used to determine contact angle from simulations in pore-space images. Here examples are shown for the Bentheimer sandstone dataset. (a) A single ganglion (red) shown in the pore space (green). (b) The fluid/fluid meniscus, the surface S_{12}, is extracted from the simulated fluid configurations. The computed Gaussian curvature, κ_G, on S_{12} is shown. (c) The contact lines (loops) are identified. These steps are applied to all the clusters (ganglia) in the image. (d) The individual ganglia shown in different colours. (e) The computed Gaussian curvature, κ_G, on S_{12}. (f) The contact lines (loops). The individual closed loops are shown in different colours. (For interpretation of the references to colour in this figure legend, the reader is referred to the web version of this article.)

Table 3
The determination of contact angle, θ, from individual clusters in pore-space images, case 4. The input contact angle is 45°. U refers to a contact angle that cannot be determined. The average value ignores the cluster for which contact angle could not be determined. We show values computed using Eq. (14) which ingores the cluster topology and solid/fluid Gaussian curvature, using Eq. (13) which includes the Euler characteristic. χ, of the clusters, and the full form of the Gauss-Bonnet equation, Eq. (3).

Cluster size (voxels)	Number of loops	Euler characteristic χ	θ (degrees) Eq. (14)	θ (degrees) Eq. (13)	θ (degrees) Eq. (3)
Beadpack					
822604	48	−5	31.0	U	U
97675	3	1	47.8	47.8	U
73496	6	1	32.0	32.0	U
65164	4	1	34.7	34.7	U
57231	8	1	21.9	21.9	131.1
56818	2	1	40.2	40.2	U
12825	1	1	95.9	95.9	U
Average			43.4		
Bentheimer sandstone					
372983	72	−1	15.5	U	U
276282	52	1	U	U	U
246618	30	0	16.8	U	U
99568	14	1	29.2	29.2	U
94948	17	1	26.9	26.9	U
89031	9	1	35.6	35.6	U
86118	9	1	41.6	41.6	U
83128	9	1	34.3	34.3	U
44527	13	1	27.3	27.3	118.2
34172	10	1	23.6	23.6	U
31718	6	1	39.6	39.6	U
23504	2	1	84.0	84.0	U
18291	4	1	48.9	48.9	U
12280	6	1	33.7	33.7	U
12169	3	1	60.1	60.1	U
10931	1	1	116.2	116.2	U
10018	4	1	50.5	50.5	U
Average			42.7		

previous work [27]. On the other hand, the solid/fluid interface, in both these simulations, and in imaging experiments, is segmented as a voxelized surface which can be rough at all length scales. Even the beadpack, for which the grains are smooth, has sharp contacts with divergent curvature. While the surface is smoothed to remove voxelization artefacts, this does not guarantee that the Gaussian curvature can be found accurately. Hence for both of the samples studied, standard image analysis methods were unable to compute the integral of the Gaussian curvature reliably, largely due to distortion near the three-phase contact line.

4. Conclusions

We have presented concepts in topology and integral geometry relevant to the study of multiphase flow in porous media. We have shown that the Gauss-Bonnet theorem does not provide a unique relationship between the integral of the Gaussian curvature of the surface of a fluid phase cluster, its topology and contact angle. We have presented, however, an approximate relationship under the assumption that the fluid–solid surface has a zero average Gaussian curvature (it is topologically flat) and is oriented, on average, in the plane of the contact line: this extends the work of [17,24] to provide a simple-to-apply relationship between topology and wettability.

We tested our theoretical analysis against lattice Boltzmann simulations of multiphase flow in porous media. We showed that when the assumptions of the analysis are valid, the contact angle can be determined accurately. When applied to simulations of residual non-wetting phase saturation in pore-space images, the average contact angle was accurate to within 3° for the cases studied. However, individual estimates for single clusters could be significantly in error because of the approximations used in the analysis.

We also showed that attempting to calculate an average contact angle from the full form of the Gauss-Bonnet theorem, including the Gaussian curvature of the solid/fluid interface was not successful, because of uncertainties in the evaluation of this curvature over a voxelized interface, even after smoothing.

Overall, the use of the Gauss-Bonnet theorem, as introduced by Sun et al. [17], does provide a useful methodology to determine an average contact angle. It is a complement to methods that evaluate curvature and contact angle geometrically from pore-space images [4,3,5]. It provides a topological counterpart to the thermodynamic contact angle that characterizes a displacement process [15].

Future work could be devoted to extending this analysis to a wider range of porous media, wettabilities, and to the analysis of experimental datasets. We could consider the analysis of wettability in mixed-wet media where the Gaussian curvature of the fluid menisci is negative [12] and for intermediate saturations where both phases are continuous throughout the image domain. It would also be of value to examine and reduce the errors in the calculation of the Gaussian curvature of solid surfaces from pore-space images [31]. Finally, it would be instructive to relate the contact angle found using our proposed expression, Eq. (14), to macroscopic flow properties, such as relative permeability and capillary pressure [24,22].

CRediT authorship contribution statement

Martin J. Blunt: Conceptualization, Data curation, Formal analysis, Investigation, Methodology, Validation, Visualization, Writing - original draft. **Takashi Akai:** Conceptualization, Data curation, Formal analysis, Investigation, Methodology, Validation, Visualization, Writing - review & editing. **Branko Bijeljic:** Conceptualization, Investigation, Methodology, Supervision, Validation, Writing - review & editing.

Declaration of Competing Interest

The authors declare that they have no known competing financial interests or personal relationships that could have appeared to influence the work reported in this paper.

Acknowledgments

References

[1] D. Wildenschild, A.P. Sheppard, X-ray imaging and analysis techniques for quantifying pore-scale structure and processes in subsurface porous medium systems, Adv. Water Resour. 51 (2013) 217–246.

[2] T. Bultreys, M.A. Boone, M.N. Boone, T.D. Schryver, B. Masschaele, L.V. Hoorebeke, V. Cnudde, Fast laboratory-based micro-computed tomography for pore-scale research: Illustrative experiments and perspectives on the future, Adv. Water Resour. 95 (2016) 341–351, https://doi.org/10.1016/j.advwatres.2015.05.012. URL www.sciencedirect.com/science/article/pii/S0309170815001062.

[3] M.G. Andrew, B. Bijeljic, M.J. Blunt, Pore-scale contact angle measurements at reservoir conditions using x-ray microtomography, Adv. Water Resour. 68 (2014) 24–31, https://doi.org/10.1016/j.advwatres.2014.02.014. URL http://www.sciencedirect.com/science/article/pii/S0309170814000372.

[4] R.T. Armstrong, M.L. Porter, D. Wildenschild, Linking pore-scale interfacial curvature to column-scale capillary pressure, Adv. Water Resour. 46 (2012) 55–62, https://doi.org/10.1016/j.advwatres.2012.05.009. URL http://www.sciencedirect.com/science/article/pii/S0309170812001443.

[5] A. Alratrout, A. Raeini, B. Bijeljic, M.J. Blunt, Automatic measurement of contact angle in pore-space images, Adv. Water Resour. 109 (2017) 158–169.

[6] M. Khishvand, A. Alizadeh, M. Piri, In-situ characterization of wettability and pore-scale displacements during two- and three-phase flow in natural porous media, Adv. Water Resour. 97 (2016) 279–298, https://doi.org/10.1016/j.advwatres.2016.10.009.

[7] A. Scanziani, K. Singh, M.J. Blunt, A. Guadagnini, Automatic method for estimation of in-situ effective contact angle from x-ray micro-tomography images of two-phase flow in porous media, J. Colloid Interface Sci. 496 (2017) 51–59.

[8] J. Schmatz, J.L. Urai, S. Berg, H. Ott, Nanoscale imaging of pore-scale fluid-fluid-solid contacts in sandstone, Geophys. Res. Lett. 42 (7) (2015) 2189–2195, https://doi.org/10.1002/2015GL063354.

[9] K.A. Klise, D. Moriarty, H. Yoon, Z. Karpyn, Automated contact angle estimation for three-dimensional x-ray microtomography data, Adv. Water Resour. 95 (2016) 152–160, https://doi.org/10.1016/j.advwatres.2015.11.006. URL http://www.sciencedirect.com/science/article/pii/S0309170815002651.

[10] L.E. Dalton, K.A. Klise, S. Fuchs, D. Crandall, A. Goodman, Methods to measure contact angles in scCO₂-brine-sandstone systems, Adv. Water Resour. 122 (2018) 278–290, https://doi.org/10.1016/j.advwatres.2018.10.020. URL http://www.sciencedirect.com/science/article/pii/S0309170818303671.

[11] Q. Lin, B. Bijeljic, R. Pini, M.J. Blunt, S. Krevor, Imaging and measurement of pore-scale interfacial curvature to determine capillary pressure simultaneously with relative permeability, Water Resour. Res. 54 (2018) 7046–7060, https://doi.org/10.1029/2018WR023214.

[12] Q. Lin, B. Bijeljic, S. Berg, R. Pini, M.J. Blunt, S. Krevor, Minimal surfaces in porous media: pore-scale imaging of multiphase flow in an altered-wettability benthiemer sandstone, Phys. Rev. E 99 (2019) 063105.

[13] A.M. Alhammadi, Y. Gao, T. Akai, M.J. Blunt, B. Bijeljic, Pore-scale x-ray imaging with measurement of relative permeability, capillary pressure and oil recovery in a mixed-wet micro-porous carbonate reservoir rock, Fuel 268 (2020) 117018, https://doi.org/10.1016/j.fuel.2020.117018. URL http://www.sciencedirect.com/science/article/pii/S0016236120300132.

[14] A.M. Alhammadi, A. Alratrout, K. Singh, B. Bijeljic, M.J. Blunt, In situ characterization of mixed-wettability in a reservoir rock at subsurface conditions, Sci. Rep. 7 (2017) 10173.

[15] M.J. Blunt, Q. Lin, T. Akai, B. Bijeljic, A thermodynamically consistent characterization of wettability in porous media using high-resolution imaging, J. Colloid Interface Sci. 552 (2019) 59–65, https://doi.org/10.1016/j.jcis.2019.05.026. URL http://www.sciencedirect.com/science/article/pii/S0021979719305648.

[16] A. AlRatrout, M.J. Blunt, B. Bijeljic, Wettability in complex porous materials, the mixed-wet state, and its relationship to surface roughness, Proc. Nat. Acad. Sci. 115(36) (2018) 8901–8906. arXiv:http://www.pnas.org/content/115/36/8901.full.pdf, doi:10.1073/pnas.1803734115. URL http://www.pnas.org/content/115/36/8901.

[17] C. Sun, E. McClure, J, P. Mostaghimi, A.L. Herring, S. Berg, T. Armstrong, R, Probing effective wetting in subsurface systems, Geophysical Research Letters 47 (5) (2020) e2019GL086151, e2019GL086151. arXiv:https://agupubs. onlinelibrary.wiley.com/doi/pdf/10.1029/2019GL086151, doi:10.1029/ 2019GL086151. https://agupubs.onlinelibrary.wiley.com/doi/abs/10.1029/ 2019GL086151.

[18] G. Garfi, C. John, S. Berg, S. Krevor, The sensitivity of estimates of multiphase fluid and solid properties of porous rocks to image processing, Transp. Porous Media 131 (2020) 985–1005, https://doi.org/10.1007/s11242-019-01374-z.

[19] G. Garfi, C.M. John, Q. Lin, S. Berg, S. Krevor, Fluid surface coverage showing the controls of rock mineralogy on the wetting state, Geophys. Res. Lett. 48 (8) (2020) e2019GL086380 arXiv:https://agupubs.onlinelibrary.wiley.com/doi/ pdf/10.1029/2019GL086380, doi:10.1029/2019GL086380. URL https:// agupubs.onlinelibrary.wiley.com/doi/abs/10.1029/2019GL086380.

[20] T. Akai, Q. Lin, B. Bijeljic, M.J. Blunt, Using energy balance to determine pore-scale wettability, J. Colloid Interf. Sci. https://doi.org/10.1016/j. jcis.2020.03.074.

[21] S. Berg, H. Ott, S.A. Klapp, A. Schwing, R. Neiteler, N. Brussee, A. Makurat, L. Leu, F. Enzmann, J.O. Schwarz, M. Kersten, S. Irvine, M. Stampanoni, Real-time 3D imaging of Haines jumps in porous media flow, Proc. Nat. Acad. Sci. 110 (10) (2013) 3755–3759. arXiv:http://www.pnas.org/content/110/10/3755.full.pdf, doi:10.1073/pnas.1221373110. URL http://www.pnas.org/content/110/10/ 3755.abstract.

[22] R.T. Armstrong, J.E. McClure, V. Robins, Z. Liu, C.H. Arns, S. Schlüter, S. Berg, Porous media characterization using minkowski functionals: Theories, applications and future directions, Transp. Porous Media 130 (2019) 305– 335, https://doi.org/10.1007/s11242-018-1201-4.

[23] H.H. Khanamiri, C.F. Berg, P.A. Slotte, S. Schlüter, O. Torsæter, Description of free energy for immiscible two-fluid flow in porous media by integral geometry and thermodynamics, Water Resour. Res. 54 (2018) 9045–9059, https://doi.org/10.1029/2018WR023619.

[24] C. Sun, J.E. McClure, P. Mostaghimi, H.A.L., M. Shabaninejad, S. Berg, R.T. Armstrong, Linking continuum-scale state of wetting to pore-scale contact angles in porous media, J. Colloid Interf. Sci. 561 (2020) 173–180. doi: https://doi.org/10.1016/j.jcis.2019.11.105. URL http:// www.sciencedirect.com/science/article/pii/S002197971931433X.

[25] L.A. Santaló, Integral Geometry and Geometric Probability, 2nd ed., Cambridge University Press, 2004.

[26] C.B. Allendoerfer, A. Weil, The Gauss-Bonnet theorem for Riemannian polyhedra, Trans. Am. Mathe. Soc. 53 (1943) 101–129, https://doi.org/ 10.2307/1990134.

[27] T. Akai, Q. Lin, A. Alhosani, B. Bijeljic, M.J. Blunt, Quantification of uncertainty and best practice in computing interfacial curvature from complex pore space images, Materials 12 (2019) 2138.

[28] M.L. Irons, The curvature and geodesics of the torus. http://www.rdrop.com/ half/math/torus/index.xhtml.

[29] T. Akai, A.M. Alhammadi, M.J. Blunt, B. Bijeljic, Modeling oil recovery in mixed-wet rocks: Pore-scale comparison between experiment and simulation, Transport Porous Media. doi:10.1007/s11242-018-1198-8.

[30] T. Akai, B. Bijeljic, M.J. Blunt, Wetting boundary condition for the color-gradient lattice Boltzmann method: Validation with analytical and experimental data, Adv. Water Resour. 116 (2018) 56–66, https://doi.org/ 10.1016/j.advwatres.2018.03.014. URL http://www.sciencedirect.com/science/ article/pii/S030917081731028X.

[31] T. Akai, B. Bijeljic, M.J. Blunt, Local capillary pressure estimation based on curvature of the fluid interface: Validation with two-phase direct numerical simulations, in: 2019, SCA-A067, Proceedings of the International Symposium of the Society of Core Analysts, Pau, France, 2019.

[32] T. Akai, M.J. Blunt, B. Bijeljic, Pore-scale numerical simulation of low salinity water flooding using the lattice Boltzmann method, J. Colloid Interface Sci. 566 (2020) 444–453, https://doi.org/10.1016/j.jcis.2020.01.065. URL http:// www.sciencedirect.com/science/article/pii/S0021979720300813.